

# Effect of paramagnetic ion concentration on proton relaxation times in aqueous copper (II) sulfate solution

Dante C. Ratchev\* and Chinmay Ambasht†

*Department of Physics, University of Illinois Urbana-Champaign, Urbana, IL, USA, 61801*

(Dated: September 25, 2025)

The relaxation behavior of nuclear spins in paramagnetic solutions provides insight into molecular dynamics and interactions between solute ions and solvent protons. In this work, we utilize nuclear magnetic resonance to study the relation between the concentration of paramagnetic ions on the spin-spin relaxation times ( $T_1$ ) and spin-lattice relaxation times ( $T_2$ ) of protons in aqueous copper (II) sulfate solution. Proton relaxation times were measured using nuclear magnetic resonance (NMR) spectroscopy across a range of copper (II) sulfate concentrations. Both  $T_1$  and  $T_2$  systematically decrease with increasing concentration which are consistent with enhanced dipole-dipole interactions and paramagnetic relaxation mechanisms. We demonstrate a quantitative relationship between the relaxation times and the concentrations. This study is relevant for understanding relaxation processes in paramagnetic systems and for applications in liquid-based nuclear magnetic resonance studies.

## I. INTRODUCTION

Nuclear magnetic resonance (NMR) was independently discovered by Felix Bloch and Edward Purcell in 1946, an achievement for which they shared the Nobel Prize in Physics in 1952 ([1]). They measured the frequencies of time-varying electromagnetic fields that caused transitions among the magnetic substates of a given solid or liquid sample. This method of spectroscopy has had a significant impact on the scientific world. It has far-reaching application to various fields beyond physics, such as medicine, geology, chemistry, and biology. Although early NMR experiments relied on continuous wave techniques, modern approaches often use pulsed NMR methods such as the Hahn echo [2] to probe spin dynamics. The most common and well-known application of NMR is magnetic resonance imaging (MRI), which produces detailed images of human tissues and diagnoses various medical issues.

In this work, we used pulsed NMR to measure the relation between the concentration of paramagnetic ions in the solution with the spin-lattice ( $T_1$ ) and spin-spin ( $T_2$ ) relaxation times in aqueous copper (II) sulfate solution. We utilized an external magnetic field to align the nuclear spins in the sample and then stimulated the system with short radio frequency electromagnetic pulses to alter the spin alignment, which allowed the measurement of the relaxation times above. In Section II, we discuss the theory and mechanism of nuclear magnetic resonance. In Section III, we describe the NMR apparatus that we used to measure the relaxation times. In Section IV, we describe the method and data collected that were used to measure the relaxation times. We describe the analysis procedures we followed in Section V to measure the various relaxation times at different concentrations. We

present the results of our analysis in Section VI. In Section VII, we conclude our main findings.

## II. THEORY

Nuclear Magnetic Resonance is a special case of a more general quantum mechanical phenomenon known as spin precession. Consider a fermion in the absence of an external electromagnetic field, the spin of the particle can have two possible orientations,  $+1/2$  and  $-1/2$ . In the presence of an external field, these states are no longer degenerate. In the presence of an external magnetic field, the Hamiltonian gains an extra term based on classical calculation of potential energy of a magnetic dipole  $\vec{\mu}$  in a magnetic field  $\vec{B}$ , of  $-\vec{\mu} \cdot \vec{B}$ . For a nuclear fermionic spin, the magnetic moment is,

$$\vec{\mu} = \gamma \hbar \vec{I} \quad (1)$$

where  $\vec{I} = +1/2$  or  $-1/2$ , is the nuclear spin and  $\gamma$  is the gyromagnetic ratio [1]. If we only apply a static magnetic field  $B_0$  in the z-direction, then the magnetic moment will precess with an angular frequency equal to the Larmor frequency  $\gamma B_0$  (Figure 1).

Now suppose we supply a time varying electromagnetic field of magnitude  $B_1$  in plane orthogonal to  $B_0$  as a perturbation to the Hamiltonian, so  $B_1 \ll B_0$ . The total magnetic field is now

$$\vec{B} = B_1(\cos(\omega t)\hat{x} - \sin(\omega t)\hat{y}) + B_0\hat{z} \quad (2)$$

Now, we change to a reference frame which is rotating at  $\omega$  along the z-axis. In our new reference frame, the z-axis remains unchanged and the effective magnetic field experienced by the spins is given by,

$$\vec{B}_{\text{eff}} = (B_0 - \frac{\omega}{\gamma})\hat{z} + B_1\hat{x}' \quad (3)$$

From this it is clear when the supplied frequency  $\omega$  is equal to the Larmor frequency  $\gamma B_0$ , the z-component

---

\* ratchev2@illinois.edu

† ambasht2@illinois.edu

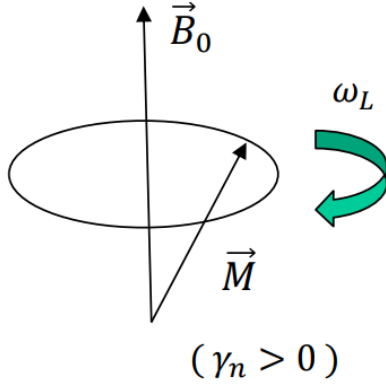


FIG. 1: Illustration of nuclear spin precession: in a static magnetic field  $\vec{B}_0$  oriented along the  $z$ -axis, the magnetization  $\vec{M}$  undergoes precession around the field direction at the Larmor frequency  $\omega_L = \gamma_n B_0$ , where  $\gamma_n$  is the gyromagnetic ratio ( $\gamma_n$  corresponds to  $\gamma$  in our equations). The figure shows the cone traced by the magnetic moment as it precesses.

vanishes— this is the resonant frequency. Thus, with the application of a transverse field which oscillates close to resonant frequency, the spins will precess around the  $x$ -axis, i.e. about  $\vec{B}_1$  with a frequency  $\gamma B_1$  (Figure 2). Hence, if this transverse field is applied for a particular time, the spin will rotate exactly into the  $x$ - $y$  plane. For a spin that points along the  $z$ -axis, the time is given by,

$$t = \frac{\pi}{2\gamma B_1} \quad (4)$$

This pulse is known as a  $\pi/2$  pulse and a pulse applied for double this time is known as a  $\pi$  pulse. Macroscopically, the net magnetic moment of all the nuclear spins can be quantified by the magnetization of the sample,

$$M = (N_\uparrow - N_\downarrow)\mu \quad (5)$$

The thermal equilibrium magnetization per unit volume for  $N$  magnetic moments is,

$$M_0 = N\mu \tanh\left(\frac{\mu}{kT}\right) \approx N\frac{\mu^2 B}{kT} \quad (6)$$

This magnetization does not appear instantaneously when the sample is placed in the magnetic field but it takes some time to build up to its equilibrium value. The differential equation that describes the rate of approach to the equilibrium is given by [1],

$$\frac{dM_z}{dt} = \frac{M_0 - M_z}{T_1} \quad (7)$$

where  $T_1$  is called the spin-lattice relaxation time. If there is no net magnetization at  $t = 0$ , then the solution to the above differential equation is given by,

$$M_z(t) = M_0(1 - e^{-\frac{t}{T_1}}) \quad (8)$$

The spin-lattice relaxation time refers to the characteristic time for the energy flow between the nuclei to the surroundings. Now, there is more than energy flow that occurs in the process of magnetization. Now suppose a  $\pi/2$  pulse is applied to a sample in thermal equilibrium. The net magnetization will be rotated into the  $x$ - $y$  plane where it will precess about the  $z$ -axis. The  $x$ - $y$  magnetization is not permanent and for most system, decays exponentially, with a characteristic time  $T_2$ , called the spin-spin relaxation time. The differential equation describing the relaxation are given by [3],

$$\frac{dM_{x'}}{dt} = -\frac{M_{x'}}{T_2} \quad \text{and} \quad \frac{dM_{y'}}{dt} = -\frac{M_{y'}}{T_2} \quad (9)$$

whose solutions are given by,

$$M_{x'} = M_0 e^{-\frac{t}{T_2}} \quad \text{and} \quad M_{y'} = M_0 e^{-\frac{t}{T_2}}. \quad (10)$$

The spin-spin relaxation time can be understood as the characteristic time period where the local fields at various proton sites affect each other. The measurement of  $T_2$  gives us information about the distribution of the local fields at the nuclear sites.

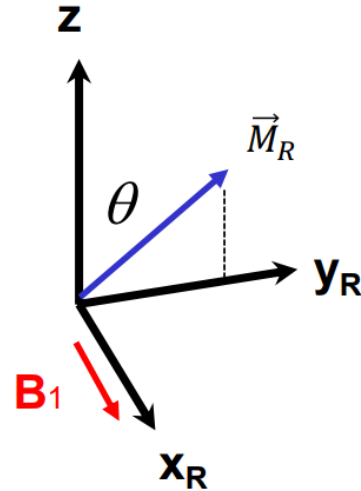


FIG. 2: Nuclear spin response in the frame rotating at  $\omega$  along the  $z$ -axis under a transverse field  $\vec{B}_1$ . In this frame, the spins precess about the  $x$ -axis (aligned with  $\vec{B}_1$ ) at a rate  $\gamma B_1$  where  $\gamma$  is the Larmor frequency. For a spin initially along  $z$ , application of  $\vec{B}_1$  for a duration  $\tau$  rotates the magnetization in the rotating frame,  $\vec{M}_R$ , into the  $x$ - $y$  plane by an angle  $\theta = \gamma B_1 \tau$ . The rotated axes  $x_R$  and  $y_R$  indicate the orientation of the rotating frame.

### III. APPARATUS

The pulsed NMR spectrometer employed in this study consists of a SpinCore iSpin-NMR system [4], a radio-frequency pulse generation and amplification chain, pro-

protective circuitry, a resonant probe circuit containing the sample, and a low-noise receiver chain for signal detection (see Figure 3). The SpinCore platform provided the pulse programming and sequencing as well as signal digitization.

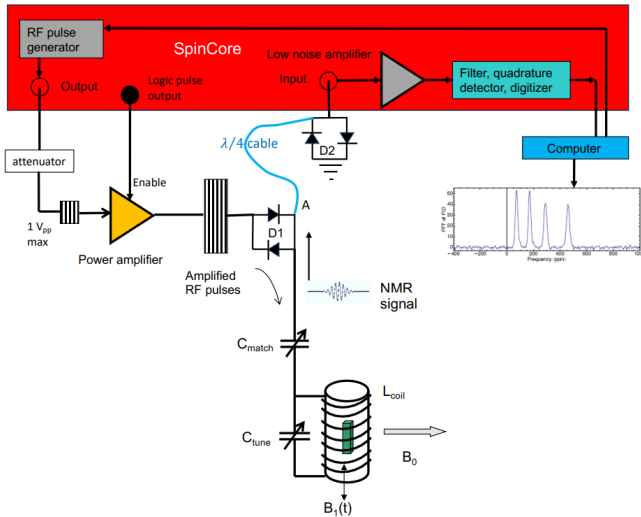


FIG. 3: Functional layout of the NMR spectrometer featuring the SpinCore iSpin-NMR system. The schematic highlights key components, including the RF amplification and transmission path, the protective diode network, the probe circuit and coil within which the sample is contained, and the receiver chain for signal detection and processing.

RF excitation pulses were generated by the iSpin-NMR system, attenuated, and then amplified to levels appropriate for transmission to the probe. The flexibility of this configuration allowed precise adjustment of pulse parameters including frequency, phase, and duration. In order to protect the receiver during high-power pulses, RF output passes through crossed diodes and a quarter-wave transmission line.

The NMR probe consisted of a coil containing the sample, coupled with variable capacitors to form an LC circuit. The main static magnetic field  $B_0$  was generated by an electromagnet driven at a constant current of 52.25 A, which corresponds to a field strength of  $B_0 = 0.7025$  T.

The coil produces the transverse magnetic field  $B_1$  that excites the nuclear spins, which precess around  $B_0$ . This precession determines the Larmor frequency, which establishes the resonance condition of the probe.

Following excitation, the precessing nuclear magnetization induces a voltage in the same coil, which generates a signal that is passed to the low-noise preamplifier where it is amplified for digitization. The computer then uses a Fourier transform to produce the frequency-domain spectrum used for further analysis.

## IV. METHODOLOGIES & DATA ACQUISITION

### A. Sample Preparation

The samples used in this study were aqueous solutions of copper (II) sulfate pentahydrate ( $\text{CuSO}_4 \cdot 5 \text{H}_2\text{O}$ ). A base solution of 0.195 M was prepared by dissolving 4.87 g of the salt in 100 mL of deionized water. A 10.00 mL aliquot of this stock was used directly as one experimental sample; additional 10.00 mL aliquots were diluted with deionized water to prepare a series of lower-concentration solutions. The final concentrations were 0.195 M, 0.0966 M, 0.0504 M, 0.0258 M, 0.0141 M, and 0.0062 M.

Measurement uncertainties were considered in both the mass of the salt and the volume of the water. The uncertainty in the mass measurement due to balance drift was estimated at  $\pm 0.05$  g, while the uncertainty in the volume measurement (also measured by mass) was  $\pm 0.05$  mL. An additional uncertainty in the addition of water of  $\pm 0.1$  mL was also included. These independent uncertainties were combined in quadrature to give  $\Delta V = \sqrt{0.05^2 + 0.1^2} = 0.1118$  mL for each measured volume. The total uncertainty in molarity was then propagated using

$$\frac{\Delta M}{M} = \sqrt{\left(\frac{\Delta m}{m}\right)^2 + \left(\frac{\Delta V}{V}\right)^2}, \quad (11)$$

and, for diluted samples prepared from a 10.00 mL aliquot, the combined relative uncertainty is

$$\frac{\Delta C}{C} = \sqrt{\left(\frac{\Delta C_{\text{stock}}}{C_{\text{stock}}}\right)^2 + \left(\frac{\Delta V_{\text{aliquot}}}{V_{\text{aliquot}}}\right)^2 + \left(\frac{\Delta V_{\text{final}}}{V_{\text{final}}}\right)^2}. \quad (12)$$

The resulting concentrations and uncertainties are presented in Table I.

TABLE I: Prepared  $\text{CuSO}_4$  solutions and uncertainties.

Uncertainties were calculated using propagation of independent uncertainties as given in Equations 11 and 12.

Concentration (M)	Uncertainty in Molarity (M)
0.195	$\pm 0.0030$
0.0966	$\pm 0.0016$
0.0504	$\pm 0.0008$
0.0258	$\pm 0.00039$
0.0141	$\pm 0.00021$
0.0062	$\pm 0.000094$

### B. Probe Tuning and Impedance Matching

Prior to each data acquisition session, the LC probe circuit was tuned and matched to minimize reflection

losses and optimize RF power transfer. A Rigol network analyzer was used to generate sinusoidal signals over a frequency range encompassing the expected Larmor frequency of 29.912 MHz, which corresponds to the precession of protons ( $^1\text{H}$ ) about  $B_0$  in the aqueous  $\text{CuSO}_4$  sample. The reflected signal was monitored using the reflection coefficient  $S_{11}$ , defined by

$$S_{11}(\text{dB}) = 20 \log_{10} \left( \frac{V_{\text{reflected}}}{V_{\text{incident}}} \right) \quad (13)$$

where  $V_{\text{incident}}$  and  $V_{\text{reflected}}$  denote the voltages of the RF signal incident on and reflected from the LC circuit. The resonant frequency of the LC circuit was identified at the frequency where  $S_{11}$  exhibited a pronounced dip.

The variable capacitors  $C_{\text{tune}}$  and  $C_{\text{match}}$  were adjusted incrementally to minimize  $S_{11}$  specifically at the target Larmor Frequency (29.912 MHz).  $C_{\text{tune}}$  controlled the resonant frequency, while  $C_{\text{match}}$  optimized the impedance match between the probe and the transmission line. Because the exact resonance frequency for pulse excitation is slightly different for each sample, the resonance frequency was later refined by locating the frequency corresponding to the maximum of the transient voltage induced in the detection coil by the precessing nuclear magnetization, also known as free induction decay (FID) signal (see Section IV C).

The tuning and matching procedure was repeated periodically, typically every few hours during extended data acquisition, to compensate for thermal or electrical drift in the circuit and to maintain the resonance throughout the measurement period.

### C. Preliminary Signal Optimization

Due to the intrinsic inhomogeneity of the electromagnet, the magnetic field at the probe was not perfectly uniform. To account for this, the orientation and position of the probe within  $B_0$  was adjusted (including translational and angular degrees of freedom) until the observed FID was maximized. This adjustment was performed prior to any LC tuning and established favorable initial conditions for subsequent measurements.

Following probe tuning and impedance matching for each sample, single RF pulses were applied repeatedly across multiple scans to determine the exact resonance frequency with an improved signal-to-noise ratio. A sufficiently long repetition delay was used between pulses to allow the nuclear spins to return to equilibrium. The FID signal was measured across a small range of frequencies near 29.912 MHz, and the frequency corresponding to the maximum FID amplitude (typically slightly offset by a few kHz) was used for subsequent pulse calibration and further experiments. The corresponding frequency-domain profile was obtained by Fourier transforming the FID signal, yielding a Lorentzian profile in the power spectral density (Figure 4).

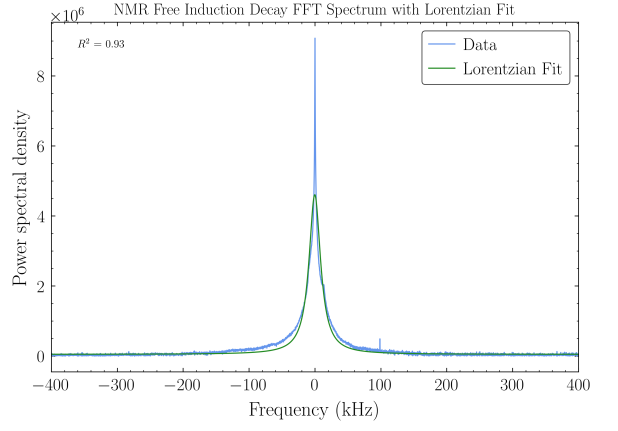


FIG. 4: Example of a frequency-domain profile obtained from Fourier transforming the free inductive decay (FID) of single pulses. The profile exhibits a Lorentzian shape, with frequency offset from the resonant frequency in kHz along the x-axis and power spectral density amplitude in a linear scale along the y-axis. The data is shown by the blue curve, and the Lorentzian fit is shown by the green curve. Example shown for the 0.0141 M sample.

### D. Pulse Calibration

With the resonance frequency established for each sample, RF pulses of various duration were applied to the LC probe. In principle, the nutation curve can be obtained by measuring the FID amplitude immediately after each pulse. However, the limited field homogeneity of the electromagnet used in this study, combined with transient effects from the RF coil and power amplifier, made direct measurement of the FID amplitude immediately following the pulses unreliable. In particular, the acquisition must begin after a short transient delay, during which dephasing due to field inhomogeneity leads to distortions in the FID.

To overcome this limitation, a two-pulse spin echo sequence was used, in which a second refocusing pulse reverses the dephasing of the spins caused by field inhomogeneities, producing a coherent echo signal that can be measured with improved accuracy. The inter-pulse delay was fixed at  $\tau = 1000 \mu\text{s}$ . The duration of the first pulse was systematically varied, while the second pulse was set to  $180^\circ$  to refocus the magnetization. The spin echo amplitude was then Fourier transformed to the frequency domain and integrated over the resonance frequency peak for each pulse length.

The integrated amplitudes were plotted as a function of pulse duration to generate a nutation curve. The nutation curves were then fitted to a sinusoidal function, and the resulting fit was used to determine the  $90^\circ$  and  $180^\circ$  pulse durations.

As the integrated FID amplitude is proportional to the transverse magnetization, the first peak of this curve corresponds to the  $90^\circ$  pulse while the first local mini-

mum following the peak corresponds to the  $180^\circ$  pulse. Consistent with previous measurements, each pulse was repeated over multiple scans with an appropriate repetition delay to allow full relaxation of the nuclear spins between pulses.(Figure 5).

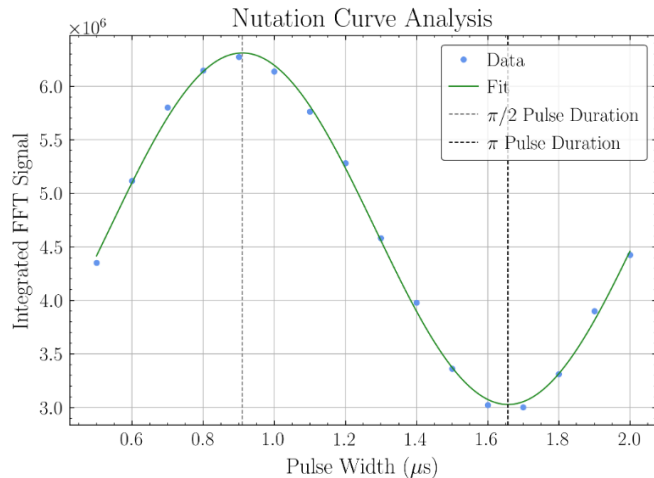


FIG. 5: Example of a nutation curve obtained by measuring the integrated FID amplitude as a function of RF pulse duration and applying a sinusoidal fit. The first peak of the curve ( $0.91 \mu s$ ) corresponds to the  $90^\circ$  RF pulse, and the first local minimum following the peak ( $1.66 \mu s$ ) corresponds to the  $180^\circ$  RF pulse. The data is given by the blue points while the sinusoidal fit is given by the green curve. Example shown for the  $1.905 M$  sample.

### E. Two Pulse NMR Experiment (Spin-Lattice Relaxation $T_1$ )

The spin-lattice relaxation time  $T_1$  of the nuclear spins was measured using a two-pulse inversion-recovery sequence. The sample was first excited with a  $\pi$  pulse to invert the net magnetization along the  $z$ -axis. After a variable recovery delay  $\tau$ , in which the magnetization relaxes back toward its equilibrium value along  $z$ , a  $\pi/2$  pulse was applied to rotate the partially relaxed magnetization into the transverse plane, generating a measurable FID signal.

The amplitude of the FID was recorded as a function of the recovery delay  $\tau$ . We then took the Fast Fourier Transform (FFT) of the FID and integrated the result over a frequency range surrounding the resonant frequency of the sample. Each measurement was repeated over multiple scans with an appropriate repetition delay between the two-pulse sequences to allow complete relaxation of the spins prior to the next  $\pi$  pulse.

The resulting integrated FID amplitudes were plotted against  $\tau$ , in which  $T_1$  was determined by fitting the data to the standard exponential recovery function described in Section II (Eq. 8).

### F. CPMG NMR Experiment

The spin-spin relaxation time  $T_2$  of the nuclear spins was measured using a Carr-Purcell-Meiboom-Gill (CPMG) pulse sequence [5, 6]. The sequence consisted of an initial  $\pi/2$  pulse to rotate the magnetization into the transverse plane, followed by a train of  $\pi$  refocusing pulses applied at regular intervals  $\tau$  to generate a series of spin echoes.

For each spin echo, the FID was recorded and Fourier transformed, and then integrated over the resonance peak. To ensure accurate measurement of transverse decay, sequences were separated by a delay sufficient for complete relaxation along  $z$ . The integrated echo amplitudes were plotted as a function of the total time from the initial  $\pi/2$  pulse to each echo, producing a decay curve.  $T_2$  was extracted by fitting this decay to the exponential model given in Section II (Eq. 10).

## V. ANALYSIS

### A. Spin-lattice relaxation times

The two-pulse NMR experiment involves first exciting the system with a  $\pi$ -pulse, then after a period  $\tau$ , the system is then excited by a  $\pi/2$ -pulse. To measure the spin-lattice relaxation times, we measured the FID signal, which was then converted into frequency space using fast Fourier transform. The transformed signal was then integrated over the frequency band to obtain the observable. The overall integrated signal is proportional to the absolute value of the magnetization measured as a function of  $\tau$ . The equation used to fit the curve is given as follows:

$$S(\tau) = |S_0(1 - 2e^{-\frac{\tau}{T_1}})| + b \quad (14)$$

, $S$  is the signal,  $b$  is the y-intercept and  $S_0$  is the amplitude of the fit. Upon analysis of the data for samples of higher concentration, we found that the data points with a shorter delay period  $\tau$  did not follow the fit given by equation (14). The aforementioned is depicted in Figure 6

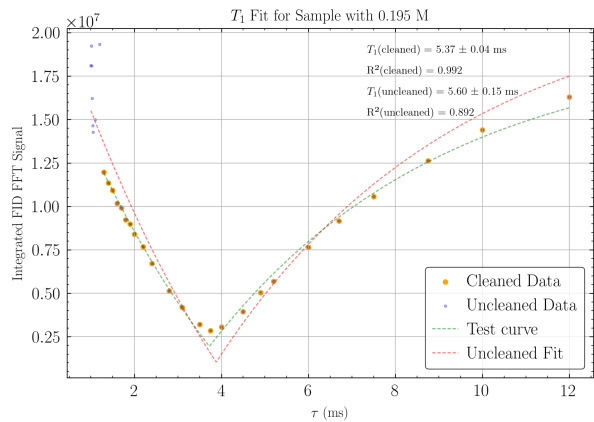


FIG. 6: Measured FFT free inductive decay signal as a function of the pulse delay time  $\tau$  in a two-pulse NMR experiment. The blue points represent the raw data obtained from the experiment and the yellow points represent the data points which better match the theoretical fit. The initial points in the raw data were discarded since these points are sensitive to external factors like voltage fluctuations, pulse reflections etc. The red curve shows the fit with entire dataset and the green curve shows the fit the cleaned dataset.

The spin-lattice relaxation time measured without discarding the data is close to the measurement with the cleaned data, hence, we can conclude that ignoring those points does not tamper with our analysis. For most curves, this deduction in the data was not required because the two-pulse NMR experiment was performed with a long delay period to not allow for any interference effects from external sources.

### B. Spin-spin relaxation times

The CPMG experiment involves first exciting the sample with a  $\pi/2$ -pulse, then we apply a  $\pi$ -pulse to excite the sample. After the first  $\pi$ -pulse, we observe spin echos in the signal and apply  $\pi$ -pulses at regular intervals to restart the process, that yields us successive spin echoes. In this experiment, a similar Fourier transform procedure is followed as in the two-pulse NMR experiment. The integrated signal is proportional to the magnetization as in the  $T_1$  experiment. The equation that is utilized to fit the data is analogous to equation (10),

$$S = S_0 e^{-\frac{\tau}{T_2}} + b \quad (15)$$

Hence, in Figure 7, we show a representative plot of the analysis that was carried out to fit the  $T_2$  data.

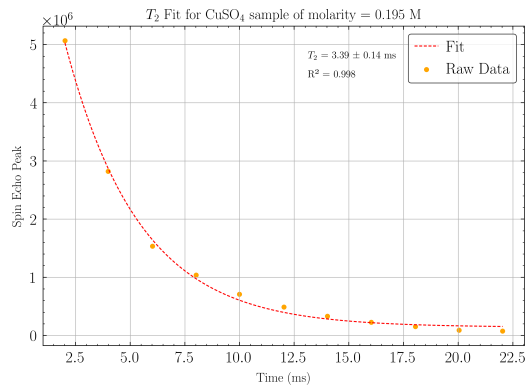


FIG. 7: Magnitude of the spin echo peak as a function of time in a Carr-Purcell-Meiboom-Gil NMR experiment. The yellow points depict the magnitude of the spin echo peak measured as a function of time. The dotted red curve represents the fit to the data. The data clearly follows an exponential trend which matches the theoretical prediction to a very good accuracy as in clearly depicted by the figure.

As we can observe in Figure 7, the theoretical fit matches the experimental data, which yields us a substantial measurement of the spin-spin relaxation time. The CPMG experiment did not produce any data which deviated from the expected results and hence as a result no data had to be removed from the final analysis.

## VI. RESULTS

Using the approaches detailed above to measure the spin-lattice ( $T_1$ ) and spin-spin ( $T_2$ ) relaxation times for each of the copper (II) sulfate samples, we observed a non-linear dependence of both  $T_1$  and  $T_2$  on solute concentration as shown in Figure 8.

Clearly, both relaxation times show a similar inverse power-law dependence on the concentration of the paramagnetic solute ( $\text{CuSO}_4$ ) and hence we can describe their approximate relation as follows,

$$T_1 \propto [\text{CuSO}_4]^{-\alpha} \quad \text{and} \quad T_2 \propto [\text{CuSO}_4]^{-\beta} \quad (16)$$

To obtain the exact values of these scaling laws we make a linear fit of the logarithm of the relaxation time versus the logarithm of the concentration. The relevant plot for the spin-lattice relaxation time is given in Figure 9.

The fitted slope of  $-1.01 \pm 0.03$  demonstrates that the dependence of  $T_1$  on concentration closely follows the power-law form given in Equation 16 with  $\alpha \approx 1$ , indicating that  $T_1$  scales nearly exactly as the reciprocal of the copper (II) sulfate concentration. The small uncertainty in the slope and high coefficient of determination ( $R^2 = 0.9811$ ) indicate high agreement between the experimental data and the log-log regression model. Fur-



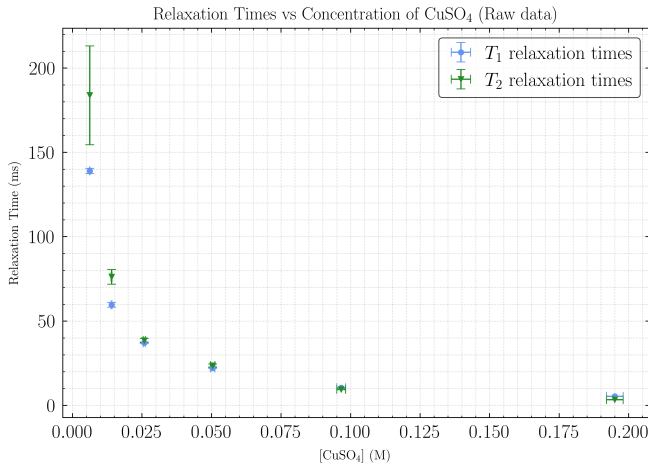


FIG. 8: Raw data for spin-lattice ( $T_1$ ) and spin-spin ( $T_2$ ) relaxation times measured for copper (II) sulfate samples, plotted against solute concentration. Both  $T_1$  (blue points) and  $T_2$  (green points) illustrate a nonlinear trend with increasing concentration.

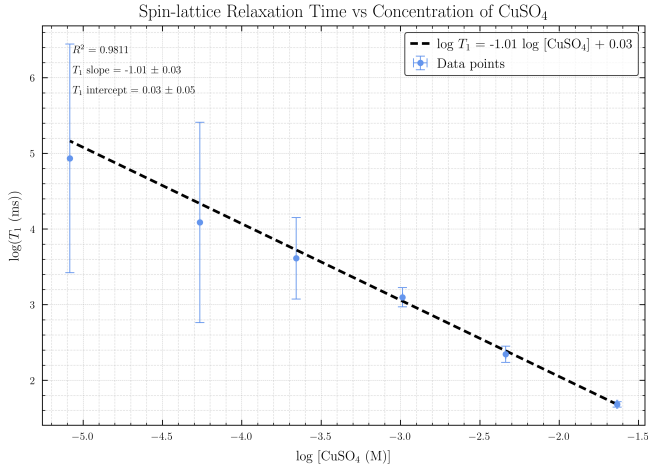


FIG. 9: Log-log plot of spin-lattice relaxation time  $T_1$  as a function of copper (II) sulfate concentration. A linear regression was applied to find a slope of  $-1.01 \pm 0.03$  and an intercept of  $0.03 \pm 0.05$ , with an  $R^2$  value of 0.9811. The data points are given in blue while the fit is given in the dotted black line. The horizontal error bars are from uncertainties in concentration calculations, while the vertical error bars represent fitting errors. The linear fit was utilized to extract the scaling law relationship.

thermore, the intercept of  $0.03 \pm 0.05$  suggests that no significant systematic offset is present.

Analogously, the spin-spin relaxation time  $T_2$  was analyzed as a function of the concentration of copper (II) sulfate using the same approach with log-log scaling, as shown in Figure 10.

A linear fit performed between  $\log(T_2)$  and  $\log[\text{CuSO}_4]$

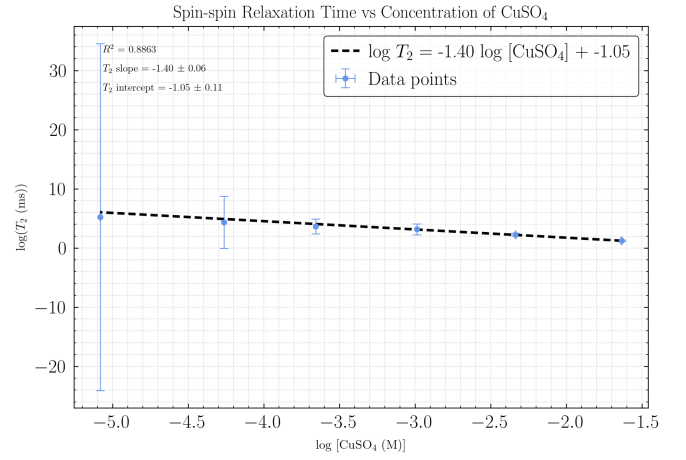


FIG. 10: Log-log plot of spin-spin relaxation time  $T_2$  as a function of copper (II) sulfate concentration. A linear regression was applied to find a slope of  $-1.40 \pm 0.06$  and an intercept of  $-1.05 \pm 0.11$ , with an  $R^2$  value of 0.8863. The data points are given in blue while the fit is given in the dotted black line. The horizontal error bars are from uncertainties in concentration calculations, while the vertical error bars represent fitting errors. The linear fit was used to extract the power law relationship.

yielded a slope of  $-1.40 \pm 0.06$  and an intercept of  $-1.05 \pm 0.11$  with a coefficient of determination  $R^2 = 0.8863$ . These results match the inverse power law relationship given in Equation 16 with  $\beta \approx 1.40$ . While the  $R^2$  value is slightly lower than for  $T_1$ , the overall trend confirms that the power-law scaling is an appropriate model for the description of  $T_2$  data across the measured concentration range.

We can additionally note that the scaling exponent of  $\beta \approx 1.40$  is greater in magnitude for  $T_2$  than that observed for  $T_1$ , reflecting a larger sensitivity of spin-spin relaxation to paramagnetic solute concentration compared to that of spin-lattice relaxation.

Both spin-lattice ( $T_1$ ) and spin-spin ( $T_2$ ) relaxation times exhibit a clear inverse power-law dependence on copper (II) sulfate concentration, with scaling exponents  $\alpha \approx 1.01$  and  $\beta \approx 1.40$  respectively. The log-log fitting analyses yield suitably high coefficients of determination ( $R^2 = 0.9811$  for  $T_1$  and  $R^2 = 0.8863$  for  $T_2$ ), indicating that the power-law model provides an accurate description of the concentration dependence. These trends reflect the underlying interactions that govern nuclear spin relaxation: as the concentration of the paramagnetic  $\text{Cu}^{2+}$  ions increase, the local magnetic environment becomes increasingly perturbed, leading to enhanced dipole-dipole interactions and magnetic field fluctuations. The observed inverse-power behavior is consistent with previous experimental and theoretical studies of paramagnetic relaxation, and provides insight into the mechanisms by which paramagnetic ions influence nuclear spin dynamics.

## VII. CONCLUSION

In this experiment, we investigated the dependence of proton relaxation times on the concentration of paramagnetic copper (II) sulfate in an aqueous solution using pulsed NMR spectroscopy methods. The spin-lattice ( $T_1$ ) and spin-spin ( $T_2$ ) relaxation times were found to systematically decrease with increasing  $\text{CuSO}_4$  concentration, following an inverse power-law relationship. This behavior is consistent with the enhanced dipole-dipole interactions and paramagnetic relaxation mechanisms expected from the unpaired electronic spins of  $\text{Cu}^{2+}$  ions, which result in the accelerated nuclear spin relaxation observed with increasing concentration. While this study focused on the effects of the presence of  $\text{Cu}^{2+}$  paramagnetic ions, the approaches taken in this paper can be extended to a broader range of paramagnetic species such as  $\text{FeSO}_4$  and  $\text{Fe}_2(\text{SO}_4)_3$ , which can be studied to create a comparison of how different electronic structures affect proton relaxation rates. Furthermore, such studies could provide valuable guidance for the interpretation of NMR data in complex chemical or material systems containing paramagnetic species.


*a. Acknowledgements:* We would like to thank Shiv Chanan and Prof. Eugene Colla for their guidance throughout the experiment. We would also like to thank Prof. Russ Giannetta for providing the additional amplifier setup to boost signal for the spin-lattice and spin-spin

relaxation measurement

*b. Author contributions:* The following contributions were made by the authors for the completion of the paper,

1. Introduction: CA
2. Theory: CA
3. Apparatus: DR
4. Methodologies and Data Acquisition: DR and CA
5. Analysis: CA and DR
6. Results: DR and CA
7. Conclusion: DR
8. Appendices: CA

### Appendix A: Analysis code and procedure

The data acquisition was done in Origin Pro 2025 and then the data was ported to comma-separated value files. This was then analyzed using python using the `numpy`, `pandas`, `scipy`, and `matplotlib` libraries. The analysis code is available on GitHub .

- 
- [1] C. P. Slichter, *Principles of Magnetic Resonance*, 3rd ed., Springer Series in Solid-State Sciences, Vol. 1 (Springer Berlin Heidelberg, 1990) pp. XII + 658, originally published by Harper & Row Publishers, New York, 1963.
  - [2] E. L. Hahn, Spin echoes, *Phys. Rev.* **80**, 580 (1950).
  - [3] A. Abragam, *The Principles of Nuclear Magnetism* (Oxford University Press, Oxford, UK, 1961).
  - [4] I. SpinCore Technologies, *iSpin-NMR Owner's Manual* (2020), accessed: 2025-09-24.
  - [5] H. Y. Carr and E. M. Purcell, Effects of diffusion on free precession in nuclear magnetic resonance experiments, *Phys. Rev.* **94**, 630 (1954).
  - [6] S. Meiboom and D. Gill, Modified spin-echo method for measuring nuclear relaxation times, *Rev. Sci. Instrum.* **29**, 688 (1958).